Supporting Information for Controlling the Dynamics and Optical Binding of Nanoparticle Homo-Dimers with Transverse Phase Gradients

Curtis W. Peterson,[†,‡] John Parker,[¶,‡] Stuart A. Rice,[†,‡] and Norbert F. Scherer[*,†,‡]

†*Department of Chemistry, The University of Chicago, Chicago, IL 60637*

‡*James Franck Institute, The University of Chicago, Chicago, IL 60637*

¶*Department of Physics, The University of Chicago, Chicago, IL 60637*

E-mail: nfschere@uchicago.edu

FORCE CALCULATIONS FOR SEVERAL PHASE GRADIENTS

We calculated the forces on each of two particles A (black) and B (red) as depicted in Figure 1a of the main text. The results are shown in Figure S1 for several regularly spaced phase gradients starting from $\xi = 0$ up to $\xi = 0.2$ in increments of $\xi = 0.025$, where $\xi = \frac{\partial \phi}{\partial R}$. Two general trends are apparent as ξ increases. The first is the force curves shift to larger force as ξ increases, corresponding to an overall larger driving force. The second is the increasing disparity in the separation dependence of the forces on each particle with increasing ξ. This progression shows the contrast between experiments with small ξ, where the optical binding locations are largely unchanged, and experiments with large ξ, where they are dramatically changed.

EXPERIMENTAL METHODS

A collimated laser beam from a Ti:Sapphire laser operating at 800nm (wavelength in vacuum) was reflected from a spatial light modulator (SLM; Meadowlark) adding a phase profile so that it formed a ring-shaped optical trap [1] when focused through a microscope objective (Olympus; APO 60x, water). A sample cell consisting of two glass cover-slips with a chamber formed by a spacer was filled with a dilute solution of 150nm dia. PVP-coated Ag nanoparticles (Ag NPs; Nanocomposix) in water. The sample was positioned so that the focus of the beam was close to the top cover slip. In this configuration the electrostatically charged PVP-coated Ag NPs become positioned close to the electrostatically charged upper glass cover slip at a distance

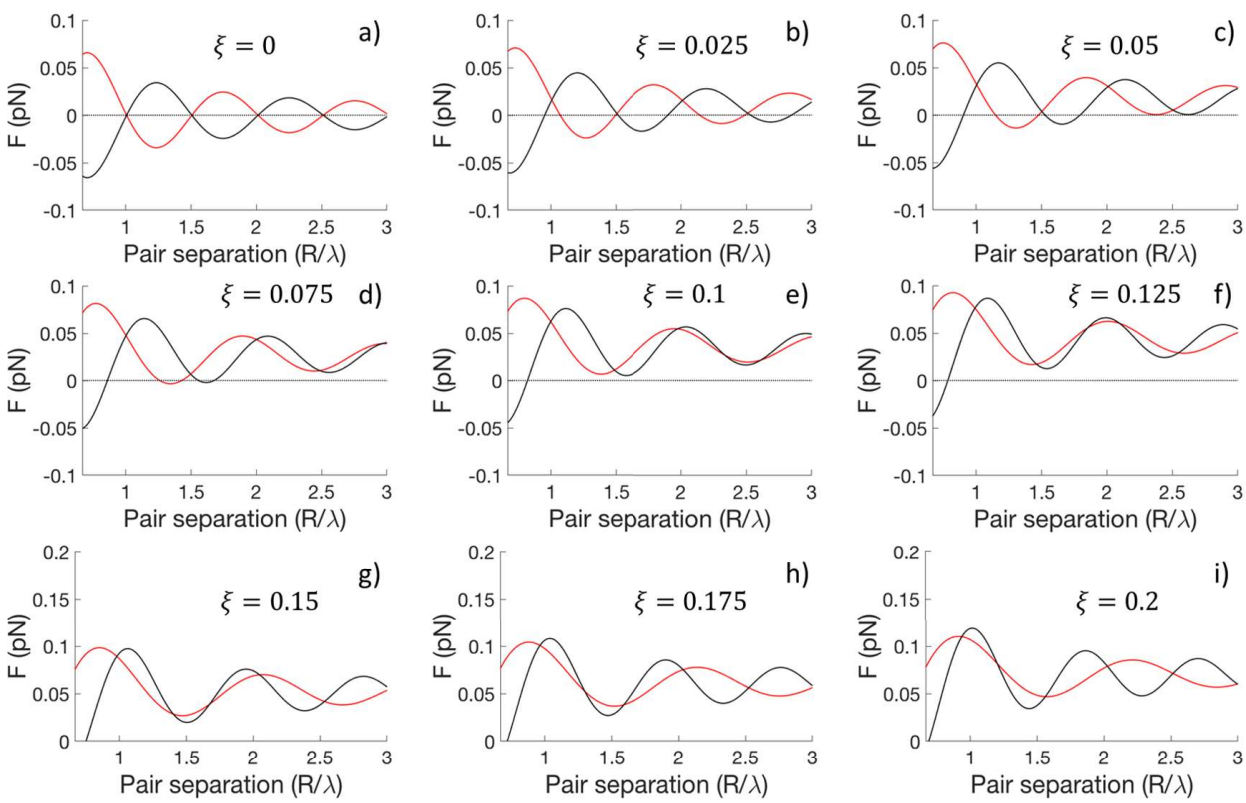

FIG. S1. (a)-(i) Calculated electrodynamic forces on two particles A (black) and B (red) for $\xi = 0$ - $\xi = 0.2$ in increments of $\xi = 0.025$.

where radiation pressure from the trapping laser is balanced by electrostatic repulsion from the cover slip [2]. The Ag NPs were, therefore, confined to a quasi-one-dimensional optical ring trap. The particles were imaged using dark-field video microscopy and tracked using the Mosaic particle-tracking suite in ImageJ. All of our experiments were carried out at low particle density (2-5 particles in the ring trap) so that our analysis could be carried out on particle pairs that were minimally disturbed by other nearby particles and our data was not conditioned on the location of a third particle. A representative example of the rad data is shown in Video S1.

An azimuthal phase gradient [2, 3] that depends on the topological charge, l, (the number of 2π phase wrappings around the ring) of the phase mask on the SLM can be added to the ring by encoding a suitable phase profile. The radius of the ring trap (r) and the phase gradient can be tuned independently, allowing a large range of experimentally accessible phase gradients to be applied.

For a sufficiently large ring, the curved path of the ring is approximately straight for distances relevant to our measurements and the direction of the phase gradient, which is tangent to the ring trap, is not much different. The periodic boundary condition of the ring trap also allows for very long trajectories to be collected under uniform intensity, polarization, and phase gradient using circularly polarized light because the relevant forces on a particle or particle pair do not depend on their angular position in the ring [4].

Phase gradient strength and parameter ξ

The explicit expression for the phase gradient parameter ξ can be derived in terms of the the magnitude of the wave vector k of the trapping light in the experimental medium (water), the topological charge l, and the ring radius r by noting that the total phase change once around the ring is

$$\Delta\phi = 2\pi l. \tag{S1}$$

Assuming that the phase varies uniformly around the circumference of the ring gives locally (over a small angular section of the ring)

$$\frac{\partial\phi}{\partial x} = \frac{2\pi l}{2\pi r} = \frac{l}{r} \tag{S2}$$

and thus

$$\xi = \frac{l}{kr}. \tag{S3}$$

In the small phase gradient regime we used a ring radius of $4.54\mu m$ with $l = 1$, $l = 3$, and $l = 5$ corresponding to $\xi = 0.021$, $\xi = 0.064$, and $\xi = 0.11$, respectively. In the large phase gradient regime we used a ring radius of $3.37\mu m$ with $l = 8$, $l = 10$, and $l = 12$ corresponding to $\xi = 0.23$, $\xi = 0.29$, and $\xi = 0.34$, respectively.

HYDRODYNAMIC INTERACTION

Our experimental and theoretical analysis is focused on electrodynamic interactions between driven nanoparticles. The hydrodynamic interactions between particles in our experiment are addressed here. The velocity of a single particle A of radius a in overdamped fluid conditions

is $\mathbf{v}_A = B_A \mathbf{F}_A$, where $B_A = (6\pi\eta a)^{-1}$ is the Stokes self-mobility of the sphere in a medium with dynamic viscosity η and $\mathbf{F}_A$ is the force on sphere A [5]. The net force on a homo-dimer, $F_{net} = F_A + F_B$, determines the dynamics of the particle pair. The velocity of the center of mass of the homo-dimer follows from Stokes' law[5] given the overdamped conditions of the experiment:

$$\langle v_{cm} \rangle = \frac{1}{2}\langle v_1 + v_2 \rangle = \frac{1}{2}\frac{F_A + F_B}{6\pi\eta a} = \frac{F_{net}}{12\pi\eta a} \tag{S4}$$

where η is the dynamic (shear) viscosity of the medium, and a is the radius of the identical particles. For electrodynamically non-interacting particles in a linear phase gradient, $F_{net} = 2F_{driving}$ and Eq. S4 gives $\langle v_{cm} \rangle = \langle v_{iso,1} \rangle = \langle v_{iso,2} \rangle$, *i.e.* the average velocity of the center of mass is equal to the velocity of an isolated particle (measured experimentally for particles that are separated by more than $3\mu m$ from their nearest neighbor) in the same phase gradient.

A second identical particle nearby B will create a flow field at particle A given by $\overline{\overline{\mathbf{H}}}(\mathbf{r}_{AB})\mathbf{F}_B$, where $\overline{\overline{\mathbf{H}}}(\mathbf{r}_{AB})$ is the Oseen tensor [6]. Following from Sokolov *et al* [7] the modified tangential velocity of particle A due to hydrodynamic interaction separated by angle $\Delta\theta_{AB}$ in our annular experimental geometry is

$$v_A^\theta(\Delta\theta_{AB}) \approx \left[B_A + g(\Delta\theta_{AB})\right] F_B^\theta; \tag{S5}$$

where

$$g(\Delta\theta_{AB}) = \frac{1 + 3\ cos\Delta\theta_{AB}}{16\pi\eta r\sqrt{2(1 - cos\Delta\theta_{AB})}} \tag{S6}$$

and r is the radius of the ring. Similarly, the radial force on particle A due to hydrodynamic interaction from the flow field caused by particle B, F_A^r, is

$$F_A^r \approx B_A^{-1} h(\Delta\theta_{AB}) F_B^\theta, \tag{S7}$$

where

$$h(\Delta\theta_{AB}) = \frac{3\ sin\Delta\theta_{AB}}{16\pi\eta r\sqrt{2(1 - cos\Delta\theta_{AB})}}. \tag{S8}$$

Eqs. S5-S8 suggest that the effects of hydrodynamic interactions can be characterized by the ratios $\chi_\theta = \frac{g(\Delta\theta_{AB})}{B_A}$ and $\chi_r = \frac{h(\Delta\theta_{AB})}{B_A}$. Fig. S2a shows plots of χ_r and χ_θ over the range of interparticle separations measured in our experiments. Although χ_r is very small throughout this range, χ_θ has a value of roughly 0.2 near single wavelength separation (*i.e.* $600nm$ for nanoparticles of radius $a = 75nm$). However, this interaction cannot give rise to the results we presented in the main text. Stable inter-particle separations will not be affected by the tangential component of the hydrodynamic interaction since $g(\Delta\theta_{AB})$ is symmetric under exchange of labels A and B, and thus any hydrodynamic forces will cancel when considering $F_B - F_A$.

Figure S2b shows a comparison between our experimentally measured pair velocities and the expected pair velocity enhancement due to hydrodynamic interaction. As in the main text, experimentally measured values of $\langle v_{cm} \rangle$ are shown as solid curves and the measured velocity of isolated particles, $\langle v_{iso} \rangle$, is shown as dashed lines. The hydrodynamically enhanced pair velocity given by $(1 + \chi_\theta)$ is shown as dotted curves. Although hydrodynamic interactions will slightly alter the tangential velocity of a particle pair, the total magnitude of this change is smaller than the enhancement of the pair velocity that we measured at separations equal to the wavelength of the trapping laser. In contrast to the monotonically decaying enhancement predicted from

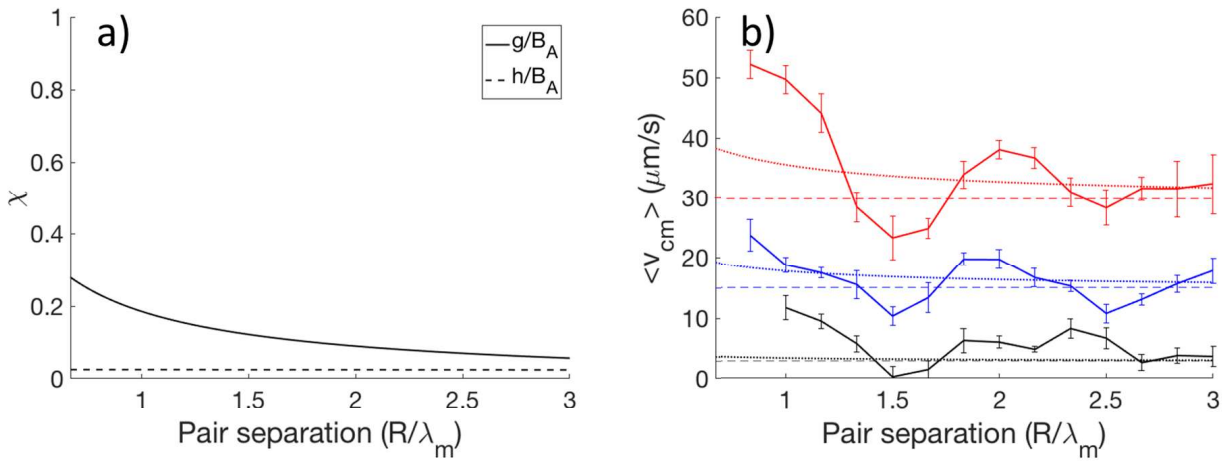

FIG. S2. Hydrodynamic interaction in particle pairs. (a) Magnitude of hydrodynamic interaction relative to the Stokes drag force as a function of pair separation in the tangential (solid) and radial (dashed) directions. (b) Comparison between our experimentally measured pair velocities and the expected pair velocity enhancement due to hydrodynamic interaction. Experimentally measured values of v_{cm} are shown as solid curves and the measured velocity of isolated particles v_{iso} is shown as horizontal dashed lines. The hydrodynamically enhanced pair velocity given by $(1 + \chi_\theta)$ is shown as monotonically decaying dotted curves.

hydrodynamics, we also measured diminished pair velocity compared to single-particle results at locations (*e.g.* $R = 1.5\lambda$) consistent with our theoretical predictions for electrodynamic interactions.

OPTICAL BINDING FOR SMALL PHASE GRADIENTS

Optical binding for small phase gradients has been covered in detail in Figliozzi *et al.*[2]. In Figure S3 we show experimentally measured particle separation PDFs (black) for $\xi = 0.021$ (a), $\xi = 0.064$ (b), and $\xi = 0.11$ (c). For comparison we have also plotted the energy (*i.e.* work) curves associated with optical binding (red). Vertical black dashed lines mark the significant minima in these energy curves, and correspond to peaks in probability. For Figure S3a-b, the first two minima are very close to $R = \lambda$ and $R = 2\lambda$, while for Figure S3c the phase gradient is strong enough to essentially eliminate the second optical binding energy minimum.

NET FORCE FOR A LARGE PHASE GRADIENT

Figure S4 shows the calculated net force in the point dipole approximation (solid) and our GMT simulations (dashed) on a homo-dimer for a large phase gradient ($\xi = 0.34$). The net force still depends on separation, but is no longer periodic and the modulations are proportionally weaker. Both of these effects can be understood from Equation 1 in the main text. Specifically, when the phase gradient is large, we expect the phase difference between the incident and scattered light at each particle to diverge from each other, *i.e.* $\Delta\phi_A \neq \Delta\phi_B$, and the interference effects that lead to the velocity enhancement for small phase gradients become much more

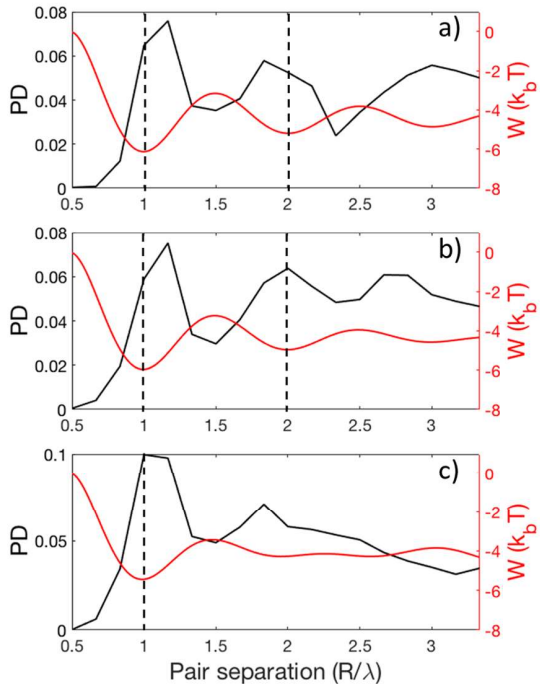

FIG. S3. (a)-(c) PDFs of measured inter-particle separations (black curves, left axis) for $\xi = 0.021$ (a), $\xi = 0.064$ (b), and $\xi = 0.11$ (c). The electrodynamic interaction potential is also plotted (red curves, right axis). The vertical dashed lines mark the significant minima in the electrodynamic interaction potential.

complicated.

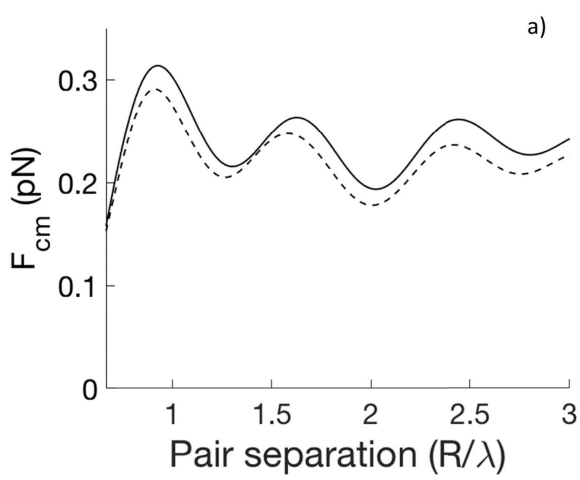

FIG. S4. Calculated net force in the point dipole approximation (solid) and our GMT simulations (dashed) on a homo-dimer for a large phase gradient ($\xi = 0.34$).

THEORETICAL POINT-DIPOLE CALCULATIONS

Describing the electromagnetic interactions in the point-dipole approximation allows employing analytical expressions for the total force on each particle. This approach provides fundamental insight into the origins of forces associated with phase differences compared to simulation methods that allow more exact calculation of the forces. We explain additional details of the theoretical model in this section.

Following the analysis of Dholakia *et al* [8], the total force on each isotropic particle along the R direction, in the point-dipole approximation, is

$$F_R^A = \frac{1}{2} Re\left[\left(\alpha_0^* \overline{\mathbf{E}}_0^{A*} + (\alpha_0^*)^2 \overline{\mathbf{E}}_0^{B*} \overline{\overline{\mathbf{G}}}^{AB*}\right) \frac{\partial \overline{\mathbf{E}}_0^A}{\partial R} + |\alpha_0|^2 \overline{\mathbf{E}}_0^{A*} \frac{\partial \overline{\overline{\mathbf{G}}}^{AB}}{\partial R} \overline{\mathbf{E}}_0^B\right], \tag{S9}$$

where α_0 is the polarizability of the identical particles, $*$ denotes complex conjugate, $\overline{\mathbf{E}}_0^A$ and $\overline{\mathbf{E}}_0^B$ are the incident electric field (vectors) at particles A and B, and $\overline{\overline{\mathbf{G}}}^{AB}$ is the dyadic Green's function that propagates the scattered field from particle B to particle A. The force on particle B can be obtained from Eq. S9 by exchanging the labels A and B. In this approximation we account for the phase gradient by explicitly plugging the phase and phase gradient derived from Eqs. S1-S2 into Eq. S9.

The polarizability of the spherical particles, α_0, is

$$\alpha_0 = \alpha_0^{'} \left(1 - \frac{2i}{3} \frac{k^3 \alpha_0^{'}}{4\pi\epsilon_m}\right)^{-1} \tag{S10}$$

with

$$\alpha_0^{'} = \frac{4\pi a^3}{3} \frac{\epsilon_m(\epsilon_p - \epsilon_m)}{\epsilon_m + \frac{1}{3}(\epsilon_p - \epsilon_m)}, \tag{S11}$$

where k is the wavevector of the light interacting with the particle, ϵ_m is the permittivity of the medium surrounding the particle, and ϵ_p is the permittivity of the particle (silver; $\epsilon_p = -30.2 + 0.387i$) [9]. Equation S9 was evaluated using Matlab at various separations, R, for the parameters $a = 75nm$ (Ag NP radius), and an incident electric field strength of $E_0 = 10^6 V/m$.

The geometry used in our analytical treatment is one-dimensional; *i.e.*, only along the inter-particle axis. However, the field is incident from a perpendicular direction. The primary complication in our experimental ring-trap geometry is that the phase varies linearly with arc-length $r\theta$ in a ring trap, while R depends the chord-length between the two particles. In analyzing our experimental particle tracking data we only considered small angular sections of the ring (*i.e.* $\Delta\theta \ll 2\pi$), where these two distances are approximately equal (*i.e.* $sin(\theta) \approx \theta$).

To make predictions related to optical binding we evaluated the work required to separate two particles from some starting distance R_1 to another distance R_2

$$W(R_2) = -\int_{R_1}^{R_2} (F_R^B - F_R^A)\, dR'. \tag{S12}$$

Optical forces are generally non-conservative [10, 11], so it is not strictly correct to call W a potential energy. However, since our system is confined to one degree of freedom, the integration

from R_1 to R_2 is guaranteed to lie on a single path, and therefore W will be a conserved quantity in the context of our experiment.

GENERALIZED MIE THEORY SIMULATIONS

Simulation Methods

The electrodynamic interactions are computed with the GMT method [12, 13] using the GMT software package MiePy that we developed. In this method, the incident and scattered fields are expanded into the vector spherical harmonic (VSH) wave functions for each particle. The incident field on particle j is expanded into the regular VSH's $\boldsymbol{N}_{nm}^{(1)}$ and $\boldsymbol{M}_{nm}^{(1)}$,

$$\boldsymbol{E}_{\text{inc}}^{j} = -\sum_{n=1}^{L_{\max}} \sum_{m=-n}^{n} iE_{mn} \left[p_{mn}^{(j\to j)} \boldsymbol{N}_{nm}^{(1)} + q_{mn}^{(j\to j)} \boldsymbol{M}_{mn}^{(1)} \right] \tag{S13}$$

where $L_{\max}$ is the maximum number of multipole orders to expand in, E_{mn} is a normalization constant, and $p_{mn}^{(j\to j)}$ and $q_{mn}^{(j\to j)}$ are the expansion coefficients of the incident source at particle j. The scattered field of particle j is similarly expanded into the scattering VSH's $\boldsymbol{N}_{nm}^{(3)}$ and $\boldsymbol{M}_{nm}^{(3)}$,

$$\boldsymbol{E}_{\text{scat}}^{j} = \sum_{n=1}^{L_{\max}} \sum_{m=-n}^{n} iE_{mn} \left[a_n^j p_{mn}^j \boldsymbol{N}_{nm}^{(3)} + b_n^j q_{mn}^j \boldsymbol{M}_{mn}^{(3)} \right] \tag{S14}$$

where a_n^j and b_n^j are the ordinary Mie coefficients [14] of particle j and p_{mn}^j and q_{mn}^j are the expansion coefficients of the light incident on particle j.

The expansion coefficients p_{mn}^j and q_{mn}^j are solved for in a system of $2NL_{\max}(L_{\max}+2)$ interaction equations

$$\begin{aligned} p_{mn}^j &= p_{mn}^{(j\to j)} - \sum_{l\neq j}^{(1,N)} \sum_{v=1}^{L_{\max}} \sum_{u=-v}^{v} A_{mn}^{uv}(l\to j) a_v^l p_{uv}^l + B_{mn}^{uv}(l\to j) b_v^l q_{uv}^l \\ q_{mn}^j &= q_{mn}^{(j\to j)} - \sum_{l\neq j}^{(1,N)} \sum_{v=1}^{L_{\max}} \sum_{u=-v}^{v} B_{mn}^{uv}(l\to j) a_v^l p_{uv}^l + A_{mn}^{uv}(l\to j) b_v^l q_{uv}^l \end{aligned} \tag{S15}$$

where $A_{mn}^{uv}(l\to j)$ and $B_{mn}^{uv}(l\to j)$ are the VSH translation coefficients from particle l to particle j.

Source decomposition in the GMT

To model the incident ring-shaped electric field, we use the following functional form of $\boldsymbol{E}$ in cylindrical coordinates,

$$\boldsymbol{E}(\rho,\theta,z) = \frac{E_0}{\rho_0^{u/2}\exp(-u/4)} \frac{\hat{\boldsymbol{x}} + i\hat{\boldsymbol{y}}}{\sqrt{2}} \rho^{u/2} \exp\left[-u \left(\frac{\rho}{2\rho_0} \right)^2 \right] \exp\left[i(l\theta + kz - \omega t) \right], \tag{S16}$$

where ρ_0 is the radius of the ring, u determines the thickness of the ring, l dictates the strength of the phase gradient (equal to l/ρ_0), and $k = 2\pi n_b/\lambda$ is the wavenumber of light in the medium

of index n_b. The normalization is chosen such that $|\boldsymbol{E}(\rho = \rho_0, \theta, z)| = E_0$. The following values were used for simulations in this work: $\lambda = 800\,\text{nm}$, $n_b = 1.33$, $E_0 = 1 \times 10^6\,\text{V/m}$, and $u = 40$. For the larger ring, $\rho_0 = 4.54\,\mu\text{m}$ and $l = 1,\ 3,$ or 5 and the for the smaller ring, $\rho_0 = 3.37\,\mu\text{m}$ and $l = 0,\ 4,$ or 8.

The incident electric field is decomposed into incident vector spherical harmonic wave functions using a near-field point matching method. [15] This provides the expansion coefficients $p_{mn}^{(j\to j)}$ and $q_{mn}^{(j\to j)}$ needed to solve the interaction equations, Eqn. S15. In this method, the coefficients are calculated so as to minimize, in a least squares sense, the difference between the expanded field, Eqn. S13, and the desired field, Eqn. S16.

Force evaluation in the GMT

Once the expansion coefficients are solved for, the time-averaged force on each particle can be determined by integrating the time-averaged Maxwell stress tensor (MST), $\langle \boldsymbol{T} \rangle$, over the surface of each sphere

$$\langle \boldsymbol{T} \rangle = \frac{1}{2}\text{Re}\left[\varepsilon_b \boldsymbol{E} \otimes \boldsymbol{E}^* + \mu_b \boldsymbol{H} \otimes \boldsymbol{H}^* - \frac{1}{2}(\varepsilon_b E^2 + \mu_b H^2)\boldsymbol{I}\right] \tag{17a}$$

$$\langle \boldsymbol{F} \rangle = \oint_\Omega \langle \boldsymbol{T} \rangle \cdot d\boldsymbol{\Omega} \tag{17b}$$

where Ω is any surface enclosing the sphere. The electric field $\boldsymbol{E}$ is calculated using the field expansions in Eqs. S13-S14 and the magnetic field $\boldsymbol{H}$ is evaluated using similar field expansions. [12]

Comparison with Theoretical Point-Dipole Calculations

The GMT results presented in the main text are in very good agreement with our theoretical model, demonstrating that the approximations made (*e.g.* point dipoles, no higher order modes, finite sizes) do not result in significant inaccuracies. The magnitude of the net forces shown in Figure 2d in the main text differ slightly for the point-dipole theory and GMT method ($< 15\%$), with the largest difference at the peaks in net force. A combination of factors affects these forces, namely: (i) higher-order multipoles in the particles due to finite size, (ii) and the more realistic electric field distribution in the GMT simulations where the *peak intensity* was set equal to the uniform intensity in our theoretical calculations.

The energy curves in Fig. 3d further demonstrate the effect of the approximations made. The shapes of the curves differ most at small separations, where multipole effects and high-order scattering are most important. There is also a slight shift of the curves that grows with separation especially for the red curves ($\xi = 0.23$) shown in Fig. 3d in the main text. This is because in our theoretical point-dipole calculations phase varies linearly with separation R, while in our GMT simulations (and experiments), phase varies linearly with arc length. For short distances these two quantities are approximately equal, but when the particles are separated by a significant angle on a circle this approximation breaks down. The relatively small shifts seen in Figure 2d in the main text demonstrate that our experiments and theoretical results were in the regime where this approximations holds relatively well.

* nfschere@uchicago.edu

[1] Y. Roichman and D. G. Grier, in *Complex Light and Optical Forces*, Vol. 6483 (International Society for Optics and Photonics, 2007) p. 64830F.

[2] P. Figliozzi, N. Sule, Z. Yan, Y. Bao, S. Burov, S. K. Gray, S. A. Rice, S. Vaikuntanathan, and N. F. Scherer, Phys. Rev. E **95**, 22604 (2017).

[3] Y. Roichman, B. Sun, Y. Roichman, J. Amato-Grill, and D. G. Grier, Phys. Rev. Lett. **100**, 013602 (2008).

[4] Y. Yifat, D. Coursault, C. W. Peterson, J. Parker, Y. Bao, S. Gray, S. A. Rice, and N. F. Scherer, Light Sci. Appl. **7**, 105 (2018).

[5] R. S. Berry, S. A. Rice, and J. Ross, *Physical Chemistry* (Oxford University Press, 2000).

[6] J. Happel and H. Brenner, *Low Reynolds number hydrodynamics: with special applications to particulate media*, Vol. 1 (Springer Science & Business Media, 2012).

[7] Y. Sokolov, D. Frydel, D. G. Grier, H. Diamant, and Y. Roichman, Phys. Rev. Lett. **107**, 158302 (2011).

[8] K. Dholakia and P. Zemánek, Rev. Mod. Phys. **82**, 1767 (2010).

[9] P. B. Johnson and R.-W. Christy, Phys. Rev. B **6**, 4370 (1972).

[10] S. Sukhov and A. Dogariu, Rep. Prog. Phys **80**, 112001 (2017).

[11] M. V. Berry and P. Shukla, J. Phys. A **46**, 422001 (2013).

[12] Y.-l. Xu, Appl. Opt. **34**, 4573 (1995).

[13] J. Ng, Z. Lin, C. Chan, and P. Sheng, Physical Review B **72**, 085130 (2005).

[14] C. F. Bohren and D. R. Huffman, *Absorption and scattering of light by small particles* (John Wiley & Sons, 2008).

[15] T. Nieminen, H. Rubinsztein-Dunlop, and N. Heckenberg, J. Quant. Spectrosc. Radiat. Transf. **79–80**, 1005–1017 (2003).